PAPER

Check for updates

Biogenic synthesis and characterization of MgO nanoparticles using *Verbascum sinaiticum*: antibacterial, free radical, and reactive oxygen species scavenging activities†

Wubshet Mekonnen Girma, [iD] *[a] Muluset Shiferaw Aragie,[a] Biniyam Abdu Berehe[a] and Ayalew H. Assen[ab]

The rapid occurrence and spread of antimicrobial-resistant bacteria pose a significant threat to global public health, increasing risks such as higher mortality rates, prolonged treatment durations, elevated healthcare costs, and reduced life expectancy. This pressing issue calls for innovative strategies to control microbial pathogens in food and environmental settings. Among these, nanomaterials have gained attention due to their exceptional durability, low toxicity, stability, and selectivity. In this study, we synthesized and characterized magnesium oxide nanoparticles (MgO NPs) using an aqueous extract of *Verbascum sinaiticum* leaves as a natural template and stabilizing agent. The crystalline nature, morphology, structural and functional groups, optical properties, stability, surface area and porosity of the synthesized Bio-MgO NPs were confirmed through X-ray diffraction analysis, scanning electron microscopy, Fourier-transform infrared spectroscopy, UV-visible spectroscopy, thermogravimetric analysis, differential scanning calorimetry, and Brunauer–Emmett–Teller analysis. We evaluated the antibacterial properties of Bio-MgO NPs against both Gram-positive and Gram-negative bacteria, including *Escherichia coli*, *Klebsiella pneumoniae*, *Listeria monocytogenes*, and *Staphylococcus aureus*. The results demonstrated promising antimicrobial activity, with highest inhibition zones of 11.10 ± 0.53 mm, 12.35 ± 0.35 mm, 10.17 ± 0.51 mm, and 10.86 ± 0.20 mm, respectively, due to synergistic effects of the plant extract and MgO NPs. These findings highlight the potential of Bio-MgO NPs as effective antimicrobial agents against a broad spectrum of bacterial strains. Beyond their antibacterial properties, the antioxidant activity of Bio-MgO NPs was also assessed using DPPH and peroxide assays. Bio-MgO NPs exhibited excellent free radical (79.8–93.9%) and reactive oxygen species (75.5–89.3%) scavenging activity, comparable to ascorbic acid, used as the standard. These results suggest that Bio-MgO NPs have immense potential for diverse applications, including biomedicine, making them a promising candidate in the fight against antimicrobial resistance.

1. Introduction

The swift rise and spread of antimicrobial-resistant bacteria present significant challenges to global public health. This issue could lead to higher mortality rates, longer treatment durations, increased healthcare costs, and reduced life expectancy. The increasing prevalence of infections caused by drug-resistant bacteria thus limits the options for effective antibiotic therapy.[1] The transmission of these pathogens from animal feces or the environment to food can happen at various stages, including harvesting, processing, distribution, and preparation.[2] Contamination with pathogens has been commonly detected in a range of food products, such as meat, fresh produce, dairy items, and ready-to-eat meals.[3] The irregular occurrence of microbial pathogens in food, along with the rising prevalence of antibiotic-resistant strains, raises significant public health concerns.[4] Hence, there is a need to develop alternative strategies for effective control of microbial pathogens in food and the environment.[5]

On the other side, human exposure to hydrogen peroxide (H_2O_2) and free radicals is notably high due to its frequent use in personal care products as a disinfectant and bleaching

[a] Department of Chemistry, College of Natural Science, Wollo University, P.O. Box: 1145, Dessie, Ethiopia. E-mail: wubshet.mekonnen@wu.edu.et; Tel: +251-910804026

[b] Applied Chemistry and Engineering Research Centre of Excellence (ACER CoE), Mohammed VI Polytechnic University (UM6P), Lot 660 – Hay Moulay Rachid, Ben Guerir, 43150, Morocco

† Electronic supplementary information (ESI) available. See DOI: https://doi.org/10.1039/d4ma01279h

agent. It is also extensively employed in industries like paper and pulp bleaching. This exposure facilitates the formation of highly reactive hydroxyl radicals ($\bullet$OH) within biological systems,[6,7] which can result in cellular damage. Additionally, H_2O_2 can be produced internally by enzymes such as superoxide dismutase. Its ability to penetrate cell membranes allows it to oxidize various cytosolic compounds.[8] Reactive oxygen species (ROS), including $\bullet$OH, are linked to a wide range of health issues, including gastrointestinal disorders, Alzheimer's disease, cancer, oxidative stress-related aging, inflammation, cell damage, and other severe conditions.[9] Reducing cellular exposure to H_2O_2 is therefore critical and can be achieved through the intake of antioxidant-rich diets and proper treatment of environmental H_2O_2 sources, such as water supplies and wastewater. In exploring potential solutions to these issues, nanomaterials have emerged as promising candidates due to their enhanced durability, reduced toxicity, greater stability, and selectivity.

Nanomaterials can be synthesized using various methods. NPs produced through natural processes, such as the use of plants as precursors or reducing agents, exhibit high biocompatibility.[10,11] These green synthesis techniques for NPs have gained significance in numerous areas of nanotechnology.[12] Various green synthesis methods utilizing biological materials, including microorganisms, marine organisms, micro-fluids, and plant extracts as reducing or capping agents, have been extensively investigated for the production of NPs.[13] Green methods for synthesizing NPs are straightforward, efficient, environmentally friendly, and cost-effective compared to traditional synthesis techniques. Additionally, the resulting products are safe for medical applications.[14,15] Plant extracts contain a variety of biologically active molecules that serve as key bio-reductants in the synthesis of NPs.[16–18] These biologically active compounds have a strong affinity for the surfaces of nanostructures and function as functionalizing ligands, enhancing the efficiency and suitability of NPs for biomedical applications.[12]

Metal oxide NPs such as ZnO, MgO, CuO, CaO, Ag_2O, and TiO_2 represent a novel class of antimicrobial agents that are gaining attention for their antibacterial properties, potential applications in food safety, environmental protection, and healthcare, and antioxidant activities.[19–21] Metal oxide NPs possess unique characteristics such as broad-spectrum antibacterial activity, a large surface area that enhances interaction with cells, a low likelihood of bacteria developing resistance, and high stability under harsh conditions. Additionally, their sizes, shapes, surface properties, and chemical compositions can be tuned, making them highly promising for the development of effective antimicrobial agents.[22]

Among these, MgO NPs have garnered significant interest due to their essential properties and importance across a wide range of fields, including physical science, chemical science, biological applications, and materials science.[23] Recently, MgO NPs have shown potential applications in medicine, particularly for conditions such as sore stomach, bone regeneration, tumor treatment, antimicrobial infections and antioxidant activity.[24,25]

In this study, leaf extracts of *Verbascum sinaiticum* were used for the first time to synthesize MgO NPs. This plant was chosen because it is widely distributed across the country and has a long-standing history in traditional medicine for treating various ailments, including diabetes, constipation, stomach issues, and skin conditions.[26,27] *V. sinaiticum*, locally referred to as "qetetina" in Ethiopia, is a biennial herb that can reach heights of 1–2 meters or more. Its stems are simple and densely covered with star-shaped hairs (stellate pubescence), giving them a pale whitish or rusty appearance. The plant's inflorescence is usually well-branched but can sometimes appear unbranched. The lower bracts are ovate and sharply pointed, measuring about 2 cm long, while the upper bracts are generally smaller. The flowers typically form clusters of 2–7, spaced apart, with pedicels ranging from 3 to 5 mm in length.[28] The key phytochemicals possessed are terpenoids, flavones, ketones, aldehydes, amides, and carboxylic acid.[29–33] Additionally, a number of phytochemicals isolated from *V. sinaiticum* reported include ajugol, luteolin, aucubin and chrysoeriol-7-glucoside.[34,35] *V. sinaiticum* plant extract has been reported for different antibacterial and antioxidant applications,[36] anti-inflammatory and analgesic activities,[37] wound healing,[38] and antidiabetic applications.[39] The primary advantage of using *V. sinaiticum* leaf extracts for the synthesis of MgO NPs lies in their accessibility, safety, and low toxicity. The leaves contain a wide range of metabolites that not only support the synthesis of MgO NPs but also facilitate a faster process as well as amplify their antibacterial and antioxidant potentials. This process is thought to occur through plant-assisted reduction, mainly driven by the various phytochemicals present in the leaves.

To the best of our knowledge, this is the first attempt to synthesize MgO NPs using *V. sinaiticum* leaf aqueous extracts as a reducing and capping agent. The obtained *V. sinaiticum* leaf extract-assisted synthesized MgO NPs (named Bio-MgO) were characterized using XRD, SEM, FTIR spectroscopy, UV-visible spectroscopy, TGA, and BET analysis and its antibacterial and antioxidant activity was evaluated. Furthermore, this study paves the way for further exploration of various indigenous Ethiopian plants for the synthesis of nanomaterials, which could be utilized in a wide range of research applications.

2. Experimental methods

2.1. Chemicals

Magnesium chloride hexahydrate ($MgCl_2 \cdot 6H_2O$, 98%), sodium hydroxide (NaOH, 99.9%), sodium phosphate dibasic (Na_2HPO_4), sodium phosphate monobasic (NaH_2PO_4), hydrogen peroxide (30% H_2O_2), 2,2-diphenyl-1-picrylhydrazyl (DDPH, >85%), methanol (CH_3OH), and dimethyl sulfoxide (DMSO) were used.

2.2. Preparation of the aqueous *V. sinaiticum* leaf extract

Leaves of *V. sinaiticum* were collected from Wollo University's Dessie campus. The leaves were air-dried at room temperature, cleaned with distilled water, and then chopped into small pieces. They were left to dry for 7 days before being ground into a fine powder using an electric grinder. 10 g of this leaf powder was then added to 500 mL of distilled water in a conical flask. The mixture was heated to 60 °C for 20 min with stirring

until all the powder was evenly mixed. After heating, the solution was allowed to cool and filtered using filter paper (Whatman filter paper), and the filtrate was collected. The resulting filtrate was used as a stock solution at different volumes for the synthesis of MgO NPs.

2.3. Preparation of the MgO NPs using a chemical method (Chem-MgO NPs)

0.2 M $MgCl_2 \cdot 6H_2O$ was added to 100 mL of distilled water. Then, it was stirred in a magnetic stirrer for 30 min and 0.5 M NaOH was added dropwise while stirring until a white precipitate appeared. Afterward, the precipitate formed was separated by centrifugation at 5500 rpm at room temperature for 20 min. Subsequently, it was washed with methanol 3–4 times to remove ionic impurities and dried in an oven for 5 h.

2.4. Preparation of *V. sinaiticum* plant extract mediated MgO NPs (Bio-MgO)

30 mL of 0.1 M $MgCl_2 \cdot 6H_2O$ solution was added to the *V. sinaiticum* leaf extract (at different volumes of 10, 20, 30, and 40 mL). Then, the mixture was stirred in a magnetic stirrer for 1 h until a dark brown solution was obtained. The precipitate formed was separated from the mixture by centrifugation at 7500 rpm and room temperature for 20 min. Subsequently, it was washed 2–3 times using distilled water. The precipitate was filtered and dried in an oven for 4 h. A schematic illustration of the synthesis of Bio-MgO NPs can be found in Scheme S1 in the ESI.†

2.5. Characterization

The XRD investigation was conducted using a Shimadzu X-ray diffractometer (XRD, Shimadzu XRD-7000) to characterize the crystallite of the MgO NPs. The surface morphology was analyzed using scanning electron microscopy (SEM) coupled with energy-dispersive X-ray spectroscopy (EDX). A TESCAN TIMA scanning electron microscope was employed for this purpose. Samples were prepared by mounting them on aluminum stubs with conductive carbon tape. An integrated EDX system facilitated quantitative elemental analysis, allowing for detailed characterization of the sample composition. The functional groups were analyzed with a PerkinElmer FT-IR spectrometer 65 FT-IR (PerkinElmer). The absorbance spectra were recorded using a DRS UV-vis spectroscopy system (Shimadzu-3600 Plus). Thermal properties were analyzed using thermogravimetric analysis (TGA) with an SDTQ600 TA instrument. The analysis was conducted over a temperature range of 25 to 850 °C, at a controlled heating rate of 5 °C min^{-1} under an airflow atmosphere. Nitrogen adsorption analyses were conducted using a 3-Flex surface characterization analyzer (Micromeritics) on evacuated, guest-free samples under pressures of up to 1 bar. The surface areas were determined by applying the Brunauer–Emmett–Teller (BET) method to the nitrogen adsorption isotherms measured at 77 K. Additionally, the pore size distribution was evaluated using the Barrett–Joyner–Halenda (BJH) method, specifically analyzing the desorption branch of the isotherm.

2.6. Antibacterial activity

The antibacterial activities of Bio-MgO NPs were investigated using the standard method Muller Hinton Agar (MHA) method. To test the antibacterial activity of Bio-MgO NPs, four bacterial strains were chosen, two Gram-negative bacteria (*Escherichia coli* and *Klebsiella pneumoniae*) and two Gram-positive bacteria (*Staphylococcus aureus* and *Listeria monocytogenes*). A sterilized nutrient broth was prepared and the turbidity of bacteria in the nutrient broth was compared with that of 0.5 MacFarland. For the disc diffusion method, the turbidity of bacteria in the nutrient broth should be equal to the turbidity of 0.5 MacFarland. The 24-hour culture of each strain was uniformly spread on a sterilized, cooled MHA medium dish, transferred to a sterile Petri plate, and set for 10–15 minutes until solidified. Then the inoculum was dispersed uniformly in MHA with a cotton swab. The sterile filter paper disk containing different concentrations of Bio-MgO NPs synthesized from the plant extract and Chem-MgO was placed on a plate containing MHA. Then, the plates were kept in a refrigerator at 5 °C for 2 h to permit diffusion and then incubated overnight at 37 °C. Then, 6 mm diameter sterile discs impregnated with Bio-MgO NP solutions (50, 100 and 200 μg mL^{-1}) were placed onto these plates and incubated for 24 h at 37 °C.

The freshly grown bacterial culture was uniformly swabbed onto the MHA plate and used for studying antimicrobial activity. The antibacterial assessment was performed and the average zone of inhibition was measured and compared with that of the control.

2.7. Antioxidant activity

2.7.1. 2,2-Diphenyl-1-picrylhydrazyl (DPPH) assay. The DPPH assay is a popular and straightforward method for evaluating antioxidant activity, often used as a starting point in such studies. DPPH is a stable, purple-colored radical that provides a clear visual indication of antioxidant action. When antioxidants are present, they donate electrons to neutralize the DPPH radical, causing the purple color to fade. This color change can be measured at a wavelength of 517 nm, with the degree of discoloration reflecting the effectiveness of the antioxidant.[40]

The antioxidant activity of Bio-MgO NPs was assessed using various concentrations of the synthesized MgO NPs, along with standard ascorbic acid (50 μg mL^{-1}, 100 μg mL^{-1}, 150 μg mL^{-1}, 200 μg mL^{-1}, and 250 μg mL^{-1}), prepared in separate test tubes. A 0.1 mM DPPH solution was prepared using methanol as the solvent. For each concentration of Bio-MgO NPs, 2 mL was mixed with 1 mL of 0.1 mM DPPH solution. The mixture was shaken vigorously and allowed to sit in a dark room for 30 min. The absorbance was measured at 517 nm, using the DPPH solution as a negative control. The antioxidant activity, expressed as percentage inhibition, was calculated using eqn (1):

$$\% \text{ of scavenging} = \frac{(\text{Absorbance of control} - \text{Absorbance of sample})}{\text{Absorbance of control}} \times 100\%$$

(1)

2.7.2. Hydrogen peroxide (H_2O_2) assay. The antioxidant activity of the sample was also evaluated using an H_2O_2 assay.
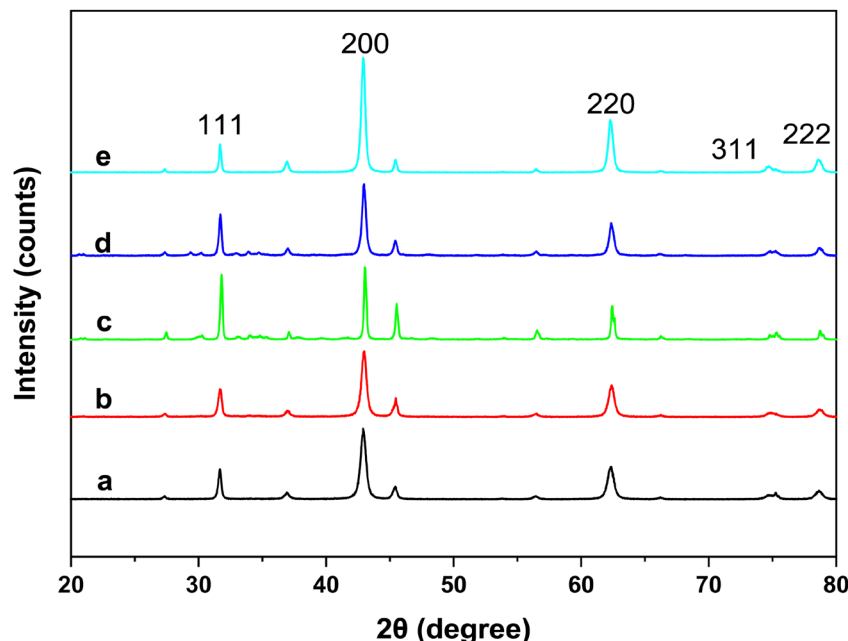
Fig. 1 XRD patterns of Bio-MgO NPs at different concentrations of the plant extract: (a) 10 mL, (b) 20 mL, (c) 30 mL, (d) 40 mL and (e) Chem-MgO.

A 40 mM solution of H_2O_2 was prepared in phosphate buffer at pH 7.4, and different concentrations of Bio-MgO NPs (50, 100, 150, 200, and 250 $\mu g \ mL^{-1}$) were prepared in separate test tubes. Each concentration of MgO NPs was mixed with 0.6 mL of the 40 mM H_2O_2 solution, using the buffer as the solvent. A total of 2 mL of each concentration of sample was combined with the H_2O_2 solution. The mixture was shaken vigorously and allowed to incubate at room temperature for 20 min. The absorbance was then measured at 230 nm, using the H_2O_2 solution as a negative control and the buffer as a blank.

The percentage scavenging activity of hydrogen peroxide was calculated using eqn (1).

2.8. Statistical analysis

Analysis of variance (ANOVA) was used to determine statistical significance. A difference was considered to be statistically significant at $P < 0.05$.

3. Results and discussion

3.1. Synthesis and characterization of Bio-MgO NPs

Bio-MgO NPs are synthesized using the *Verbascum sinaiticum* plant extract by first collecting, drying, and grinding the plant into a fine powder. The powder is extracted in an aqueous system to isolate bioactive compounds, which are then mixed with magnesium chloride hexahydrate ($MgCl_2 \cdot 6H_2O$). The extract's biomolecules act as reducing and stabilizing agents to form Bio-MgO NPs, which are collected, characterized, and evaluated for various applications (Scheme S1, ESI†). The phase purity and crystallite of the as-synthesized MgO NPs were analyzed by XRD. Fig. 1 presents the XRD patterns of MgO NPs synthesized *via* chemical methods (Chem-MgO) and

V. sinaiticum leaf extract-assisted methods (Bio-MgO). The XRD patterns for all MgO NP samples exhibited peaks at 2θ values of 32.34°, 43.52°, 62.6°, 75.4°, and 79.24°, corresponding to the (111), (200), (220), (311), and (222) diffraction planes, respectively (JCPDS 045-0430). As shown in Fig. 1a–e, all samples displayed identical XRD diffraction patterns, confirming the crystalline nature of the MgO NPs. The results indicate that the plant extract did not alter the crystallite structure of MgO NPs, consistent with the findings reported in the literature.[1,41]

The average crystalline (D) diameter was calculated using the Scherrer equation (eqn (2)).

$$D = \frac{k\lambda}{\beta \cos \theta} \tag{2}$$

where D is the crystallite size in nanometer (nm), k is the Scherrer constant (0.94 and 0.89 for homogeneous and heterogeneous samples, respectively), λ is the wavelength of the X-ray source (Cu Kα radiation = 1.5406×10^{-10} m), β is the full-width at half maximum (FWHM) of the X-ray profile in radian and θ is the diffraction angle in radian.

The average crystallite size of Chem-MgO NPs was calculated to be 17.8 nm and for Bio-MgO synthesized at 10, 20, 30, and 40 mL, it was found to be 19.6, 15.4, 18.4, and 18.9 nm, respectively. These variations arise from differences in synthesis methods, plant extract concentrations, and the influence of lattice strain and defects. In bio-synthesis, biomolecules (*e.g.*, polyphenols, flavonoids) act as reducing, capping, and stabilizing agents, affecting nucleation and growth. Lower extract concentrations (10 mL) result in slower nucleation and larger crystallites (19.6 nm), while higher concentrations (20 mL) enhance nucleation, yielding smaller crystallites (15.4 nm). At 30 mL, a balance between nucleation and growth leads to moderately sized crystallites (18.4 nm), whereas
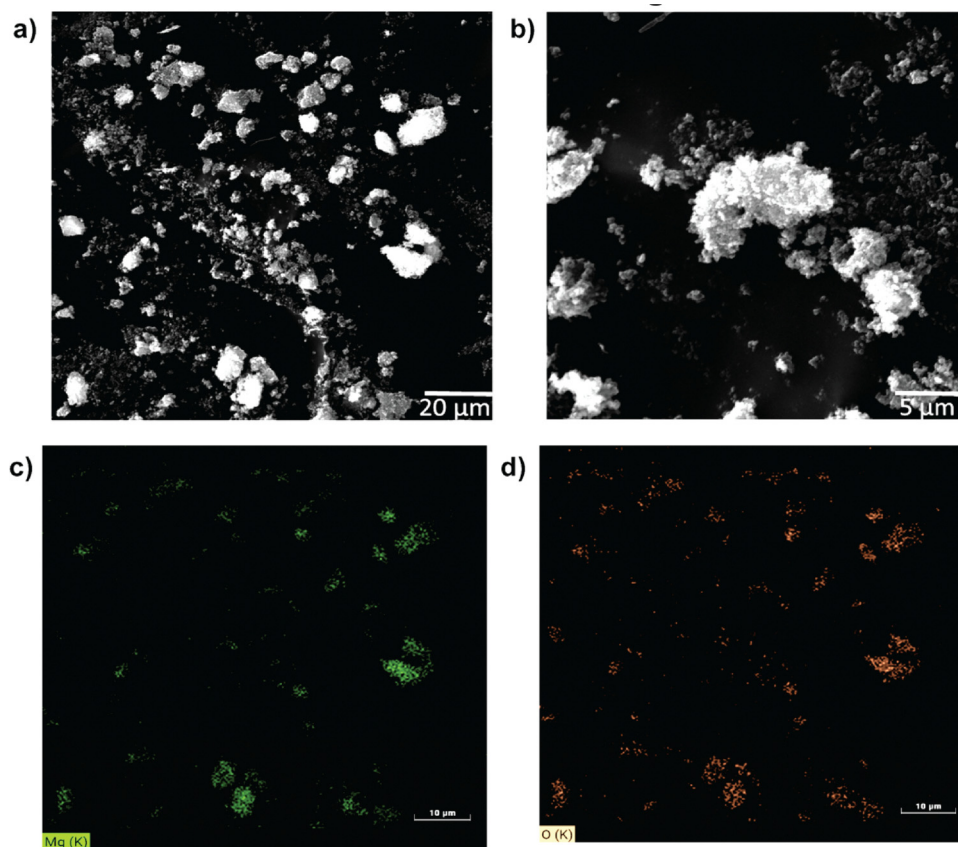
Fig. 2 The SEM images of Bio-MgO NPs (a) and (b) EDS mapping of (c) Mg and (d) O.

excessive biomolecules at 40 mL may cause over-capping or agglomeration, slightly increasing the crystallite size (18.9 nm) and introducing defects.[42,43]

The morphology of the samples was assessed using SEM analysis. Fig. 2a and b show that the MgO NPs are agglomerated and appear as spherical and irregular individual particles. The rough and uneven surface topography shown is evidence for the agglomerated MgO NPs. The distinct microstructures are evidence for the inherent porous nature of the synthesized NPs. Furthermore, the SEM image signifies the brighter and darker areas representing dense or electron-rich and voids or less dense regions, respectively. The EDS mapping in Fig. 2c signifies the uniform distributions of Mg in the NP cluster, confirming that the primary constituent element is Mg. The signal intensity variations indicate differences in the particle size and the heterogeneity of the NPs, which contributes to the agglomerated nature of MgO NPs. In Fig. 2d, the EDX mapping showed that the O distribution well aligns with the Mg distribution, indicating the presence of Mg and O in a stoichiometric ratio. A minor variation in O intensity may indicate slight surface adsorption of environmental species, such as moisture or impurities, which is typical for highly reactive MgO NPs.

The surface functional groups present in MgO NPs synthesized at different plant concentrations were investigated using FTIR analysis. The crude plant extract and Chem-MgO NPs were also analyzed as a control. Fig. 3a shows the FTIR spectra of 10,

20, 30, and 40 mL of Bio-MgO, Chem-MgO and the plant extract, respectively. In Fig. 3a, the FTIR spectra of all Bio-MgO samples and the plant extract show major stretching peaks at 3350, 2935, 1643, 1432, 1103, and 851 cm^{-1}.[44,45] The presence of peaks around 3350 cm^{-1} signifies the searching vibrations of O–H from water molecules or plant biomolecules like alcohol or phenol. Peaks that appear around 2935 cm^{-1} are attributed to C–H stretching vibrations from the plant extract. The peak around 1643 cm^{-1} represents C=O stretching groups likely from amides, carboxylic acids or carbonyl groups. The peak around 1432 cm^{-1} is more likely assigned to the C–H deformation. The peak around 1103 cm^{-1} is assigned to C–O or Mg–O–C stretching vibrations from residual organic matter or plant metabolites.[1] In particular, the peaks corresponding to 850–900 cm^{-1} are characteristic of Mg–O stretching vibrations, confirming the formation of MgO NPs.[46] The peaks in the low frequency region below 500 cm^{-1} are attributed to Mg–O vibrations, reinforcing the structural integrity of the synthesized MgO NPs. The FTIR spectra of Chem-MgO display a major peak around 921 and one below 500 cm^{-1} associated with the stretching vibrations of Mg–O.

The absorbance spectra of 10, 20, 30, and 40 mL of Bio-MgO, Chem-MgO and the plant extract were obtained in the absorbance range of 200–800 nm as shown in Fig. 3b. All synthesized samples showed a non-zero absorbance from 200 nm extending to longer wavelengths. However, as the concentration of the
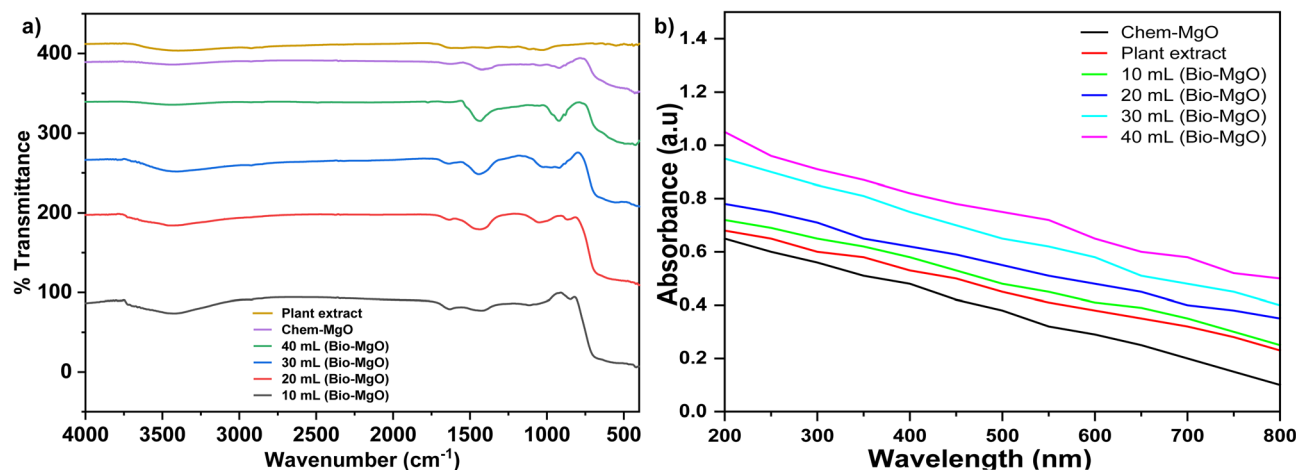
Fig. 3 (a) FTIR spectra and (b) the absorbance of Chem-MgO and Bio-MgO NPs.

plant extract increased during the synthesis of MgO NPs, its absorbance also increased due to the synergistic absorbance effect of both the plant extract and MgO NPs.

The stability of the synthesized MgO at different plant concentrations was illustrated using thermogravimetric analysis (TGA) and differential scanning calorimetry (DSC) curves (Fig. 4a–e). In the first stage of Chem-MgO, a 14.4% weight loss, occurring below 200 °C, corresponds to the removal of adsorbed water molecules and volatile organic impurities (Fig. 4a). The DSC curve indicates that this process is endothermic. In the second stage, a weight loss of around 11.6% might be due to the loss of adsorbed organic impurities. In the third stage at higher temperatures, the weight loss around 14% might be due to the removal of chemically bonded hydrogen and carbonate from atmospheric carbon dioxide adsorbed during synthesis. From the DSC curve, the second and third stage weight loss takes place through an exothermic process. In Fig. 4b–e, Bio-MgO synthesized at different plant concentrations 10, 20, 30, and 40 mL showed a weight loss at first stage 9, 4.3, 5.6, and 4.4%, respectively, associated with the evaporation of moisture and loosely bound water molecules. In the second stage, a weight loss of 4.3, 3.1, 3.2, 3.8, and 8.9% was observed more likely due to the decomposition of organic matter introduced from biosynthesis using *V. sinaiticum*. In the third stage, samples showed a weight loss of 14.3, 7.9, 9.7, and 8.9% indicating thermal degradation of strongly bound organic matters and carbonates. From the DSC curves, it is evident that all Bio-MgO NPs' first, second and third-stage weight losses took place through endothermic, exothermic and exothermic processes, respectively (Fig. 4b–e). In general, the TGA curves that demonstrated the synthesis of Chem-MgO using chemical methods showed higher weight loss related to the presence of impurities in the course of synthesis. However, among Bio-MgO, 20 mL Bio-MgO showed a lower weight loss indicating more efficient capping and thinner organic matter in the MgO NP surface.

The Brunauer–Emmett–Teller (BET) analysis results provide information about the surface area and porosity of MgO NPs synthesized using chemical and biological methods. As shown

in Fig. 5a, the adsorption/desorption curve of Chem-MgO NPs shows a characteristic Type IV isotherm with a hysteresis loop at higher relative pressures ($P/P_0 > 0.8$), indicating a mesoporous structure.[47,48] A moderate surface area about 23 m^2 g^{-1} suggests the presence of particles with relatively uniform mesoporosity. The adsorption isotherms of the biosynthesized MgO (Bio-MgO) NPs, 10, 20, 30, and 40 mL Bio-MgO NPs in general, show enhanced nitrogen uptake compared to Chem-MgO, particularly at intermediate pressures (P/P_0). All samples show Type IV isotherms with hysteresis loops, characteristic of mesoporous materials. The surface area of 10, 20, 30, and 40 mL Bio-MgO NPs is 30, 14, 21, and 13.5 m^2 g^{-1}, respectively. These results suggest that 10 mL Bio-MgO and 30 Bio-MgO relatively showed higher surface areas compared to Chem-MgO and other Bio-MgO NPs. Among all samples 40 mL Bio-MgO exhibits a lower surface area, indicating that increasing the plant extract initially leads to an increase in the organic content, which reduces the surface area and aggregation pore blocking. The surface area improves with 30 mL Bio-MgO NPs, likely due to a balanced pore structure that may enhance stability for specific applications. This result suggests that during the synthesis of bio-mediated MgO NPs, optimization of the plant extract concentration is important to maximize the performance in the real applications of NPs.[49] The BET pore distribution curves (Fig. Sa–e, ESI†) illustrate the differential pore volume (dV/dW, cm^3 g^{-1} nm^{-1}) as a function of pore width (nm) for Chem-MgO and Bio-MgO synthesized using varying volumes of the *V. sinaiticum* plant extract (10 mL, 20 mL, 30 mL, and 40 mL, respectively). The BET pore distribution analysis reveals that MgO samples synthesized with the *V. sinaiticum* plant extract exhibit varying pore characteristics depending on the extract volume. Chem-MgO shows a uniform mesoporous structure with a peak pore volume of 0.21 cm^3 g^{-1}. The 10 mL Bio-MgO sample has a broader pore distribution (up to 120 nm) and higher pore volume (0.35 cm^3 g^{-1}), indicating a more heterogeneous structure.[50] Increasing the extract volume to 20 mL results in a narrower, more uniform mesoporous
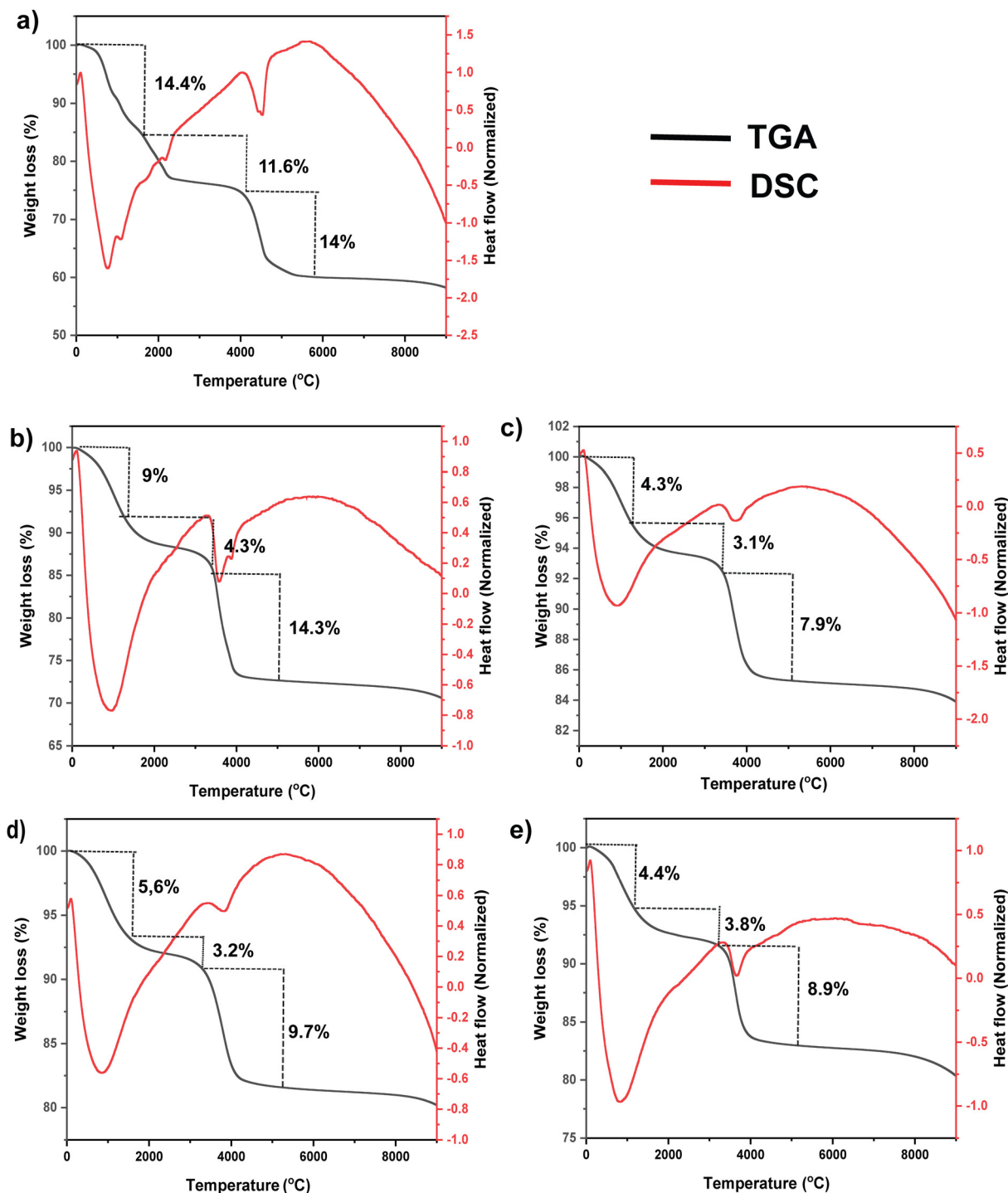
Fig. 4 The TGA and DSC curves of (a) Chem-MgO, (b) 10 mL Bio-MgO, (c) 20 mL Bio-MgO, (d) 30 mL Bio-MgO and (e) 40 mL Bio-MgO.

distribution with a peak at 0.10 cm^3 g^{-1}. The 30 mL and 40 mL samples show stable mesoporous structures but with reduced pore volumes (0.15 cm^3 g^{-1} and 0.12 cm^3 g^{-1}, respectively), suggesting denser structures at higher extract concentrations. These findings highlight the role of the *V. sinaiticum* extract in modifying MgO NP pore properties, with lower volumes favoring broader distributions and higher volumes leading to more uniform but less porous structures. In general, 10 mL Bio-MgO showed a higher surface area (30 m^2 g^{-1}) due to an optimal balance of particle size and pore structure, with minimal pore blocking. However, 20 mL Bio-MgO displayed a lower surface area (14 m^2 g^{-1}) despite a smaller particle size (15.4 nm) due to increased organic residues, NP aggregation, and potential pore blocking or collapse. The TGA and BET data highlight the complex role of the plant extract concentration in determining the textural properties of Bio-MgO NPs.
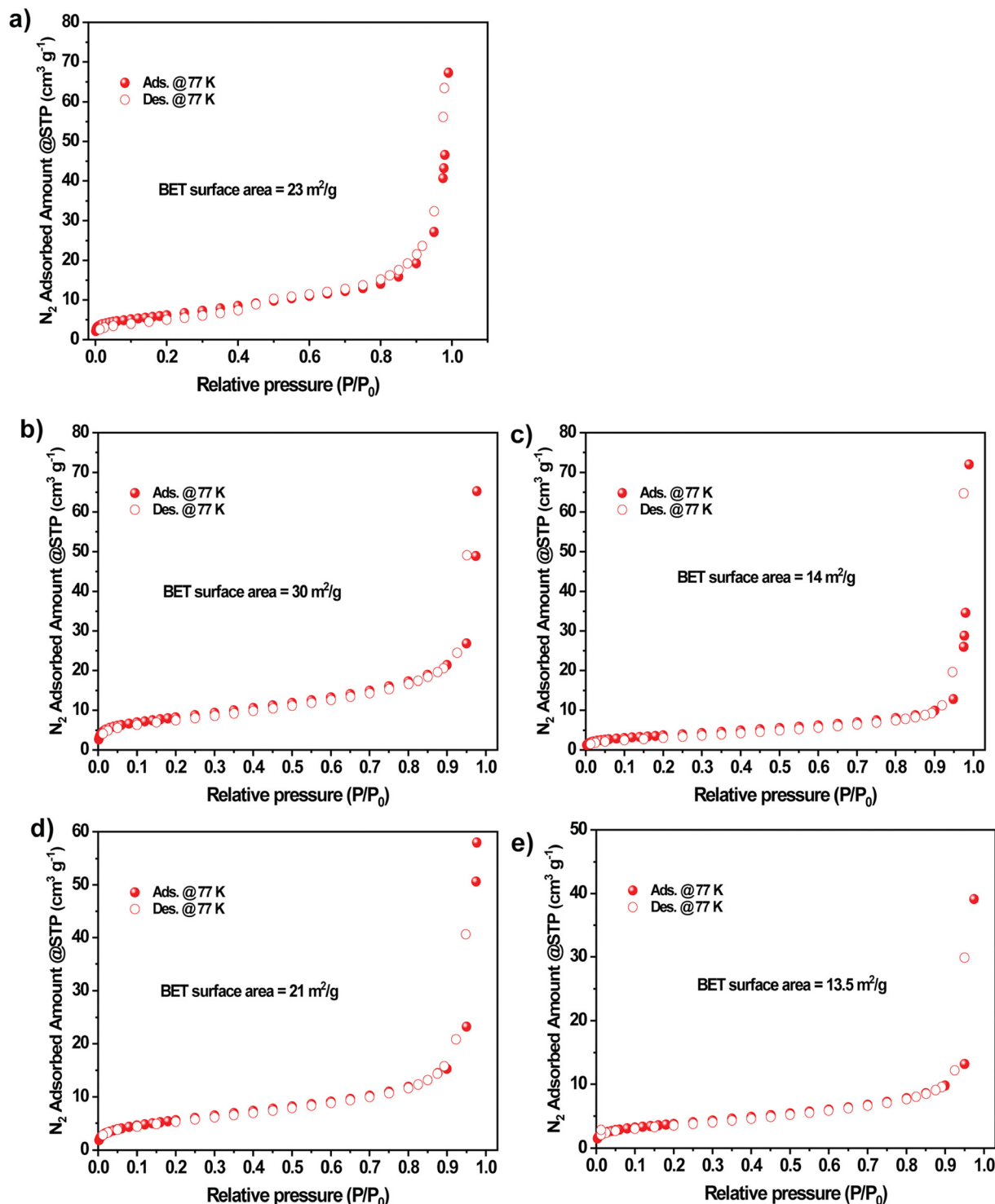
Fig. 5   The BET surface area of (a) Chem-MgO, (b) 10 mL Bio-MgO, (c) 20 mL Bio-MgO, (d) 30 mL Bio-MgO and (e) 40 mL Bio-MgO.

3.2.   Antibacterial performances of Bio-MgO NPs

Antibacterial activity was examined using the disc diffusion method.[51] To examine the antibacterial activity of Bio-MgO NPs synthesized using the *V. sinaiticum* leaf extract assisted technique, four bacterial strains were chosen, two Gram-negative bacteria (*E. coli* and *K. pneumoniae*), two common human

pathogens that cause a wide spectrum of infections, and two Gram-positive bacteria (*S. aureus and L. monocytogenes*), two main foodborne pathogens (Fig. 6a–d). The antibacterial activity of Bio-MgO NPs was tested at various concentrations (50, 100, and 200 μg mL^{-1}) by incubating the Bio-MgO NP sample for 24 h at 37 °C (Fig. 7a–f). For comparison experiments, the crude plant

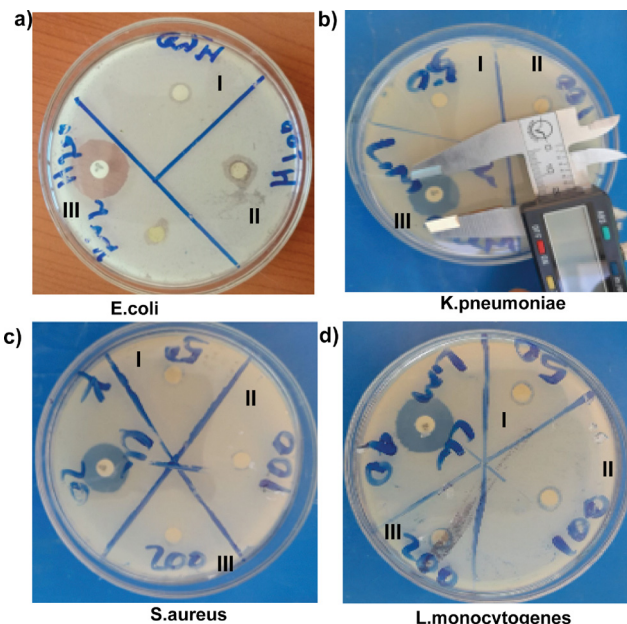© 2025 The Author(s). Published by the Royal Society of Chemistry

Fig. 6 Antibacterial activity of Bio-MgO NPs against (a) *E. coli*, (b) *K. pneumoniae*, (c) *S. aureus*, and (d) *L. monocytogenes* (I = 50, II = 100, and III = 200 µg mL^{-1} of the Bio-MgO NP dose).

extract and Chem-MgO were also examined. For positive control, chloramphenicol was used as a standard antibacterial agent, while DMSO was used as a solvent. The zone of inhibition for control (chloramphenicol) against *E. coli*, *K. pneumoniae*, *S. aureus* and *L. monocytogenes* bacterial strains was 19.97 ± 0.25, 21.76 ± 0.5, 16.10 ± 0.21, and 21.14 ± 0.35 mm, respectively.

After incubation, the zone of inhibition was measured to assess the inhibitory activity of the Bio-MgO NPs (Fig. 6a–d and Table S1, ESI†). The results revealed that as the concentration of Bio-MgO NPs increased, the zone of inhibition also increased against both Gram-positive and Gram-negative bacterial strains (Fig. 7a–d and Table S1, ESI†). The highest zones of inhibition were recorded for 40 mL Bio-MgO NPs (200 µg mL^{-1}) incubated with *E. coli*, *K. pneumoniae*, *S. aureus*, and *L. monocytogenes*, 11.1 ± 0.53, 10.86 ± 0.20, 10.17 ± 0.51, and 12.35 ± 0.35 mm, respectively (Fig. 7d). This suggests that this concentration optimizes features essential for antimicrobial effectiveness. Bio-MgO NPs typically exert antibacterial effects through mechanisms such as ROS generation, direct interaction with bacterial cell walls, and the release of Mg^{2+} ions, which disrupt cellular processes.[52,53] At 40 mL, the Bio-MgO NPs exhibit a surface area of 13.5 m^2 g^{-1}, the lowest among the bio-synthesized samples, along with a broader pore size distribution as indicated by pore distribution analysis in Fig. S1 (ESI†). Despite the lower surface area, the higher extract concentration may result in increased incorporation of bioactive compounds from *V. sinaiticum* on the NP surface, potentially enhancing ROS production or surface reactivity. Furthermore, the smaller crystallite size observed at higher extract concentrations (though optimal at 20 mL, the trend may persist to some degree) could improve the surface-to-volume ratio, enabling more efficient interactions with bacterial cells, even with a reduced BET surface area.[54] All the results show a dose-dependent antibacterial activity in both Gram-positive and Gram-negative bacteria. A similar trend is observed in Chem-MgO NPs and the bare crude extract (Fig. 7e–f). The results indicate that *E. coli* and
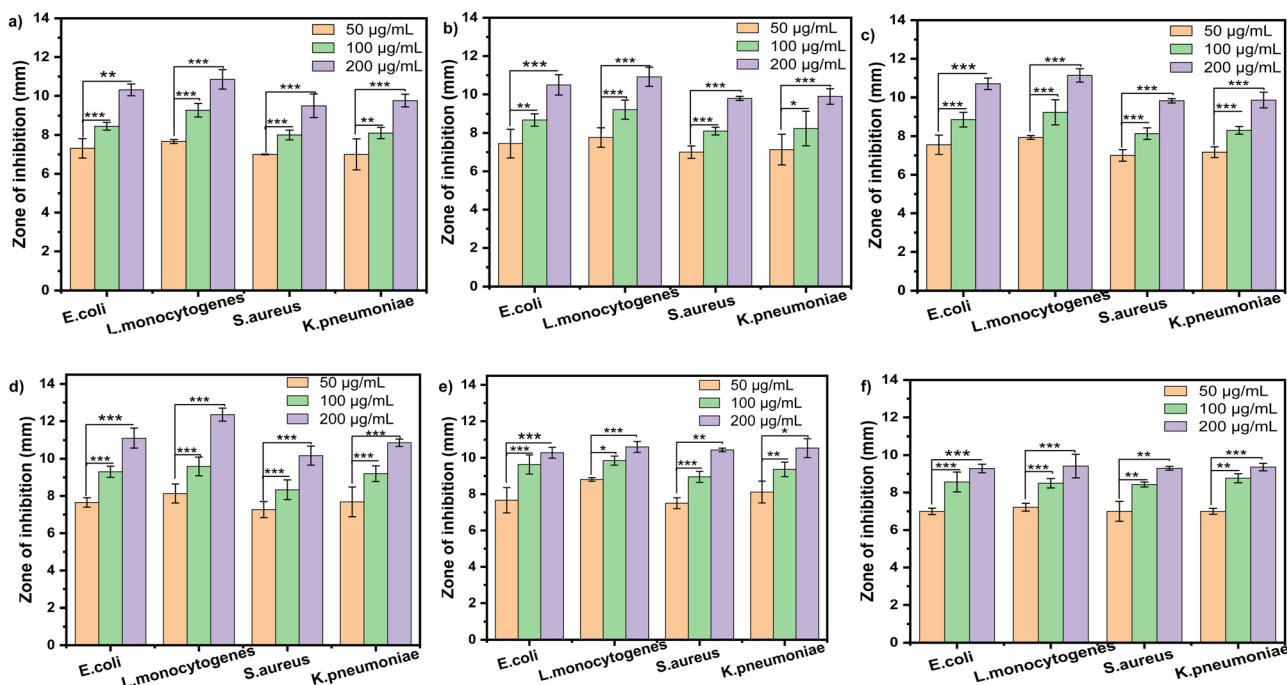

Fig. 7 The antibacterial activities of (a) 10 mL Bio-MgO, (b) 20 mL Bio-MgO, (c) 30 mL Bio-MgO, (d) 40 mL Bio-MgO, (e) Chem-MgO and (f) plant extract. Error bars indicate the mean ± standard deviations (*n* = 3).
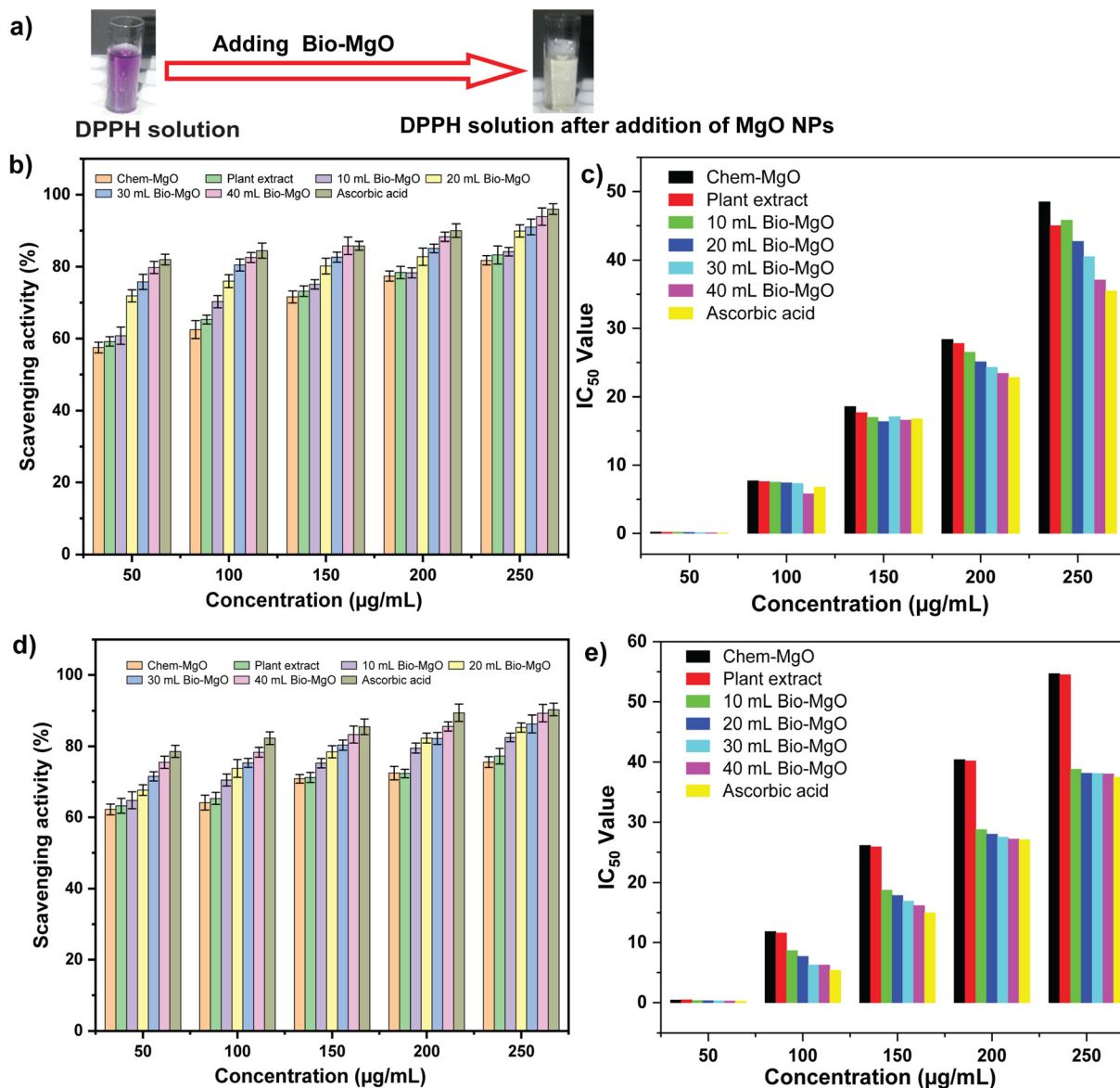
Fig. 8 (a) Photographs of DPPH before and after incubation of Bio–MgO NPs, (b) free radical scavenging using the DPPH assay, (c) IC_{50} value calculated from the DPPH assay, (d) ROS scavenging activities using the H_2O_2 assay and (e) IC_{50} value calculated from the H_2O_2 assay using different samples. Error bars indicate the mean $\pm$ standard deviations (n = 3).

L. monocytogenes are highly susceptible to Bio-MgO NPs, showing greater sensitivity compared to other tested bacteria (Fig. 7a–d and Table S1, ESI†), which could be due to the differences in the bacterial membrane structure. Similarly, Chem-MgO (Fig. 7e) and the plant extract (Fig. 7f) showed similar sensitivity towards *E. coli* and *L. monocytogenes*; however as compared to the Bio-MgO NPs, they showed lower antibacterial activities. The results of the antibacterial activity were consistent with the findings from previous studies.[55–57] The mechanism of antibacterial activity involves the penetration of Bio-MgO NPs through the bacterial cell membrane, causing membrane damage that ultimately leads to cell death. This interaction between Bio-MgO and the bacterial membrane is attributed to their nanoscale size and high surface-to-volume ratio.[58] The interaction of Bio-MgO NPs with the bacterial membrane could be due to the large surface-to-volume ratio.

3.3. Free radical and ROS scavenging activity of Bio-MgO NPs

The free radical scavenging activity of Bio-MgO NPs was tested using a DPPH assay using ascorbic acid as a positive control and Chem-MgO NPs and plant extract as negative controls. The DPPH solution is purple due to the presence of free radicals on nitrogen atoms. However, upon incubating with an antioxidant (Bio-MgO NPs), the free radicals are neutralized by the addition of hydrogen or electrons, causing the solution to change from purple to colorless (Fig. 8a). This visual evidence suggests that Bio-MgO NPs possess antioxidant properties, as effective antioxidants neutralize free radicals, leading to decolorization of

the DPPH solution. To demonstrate the antioxidant capabilities of Bio-MgO NPs by incubation of various concentrations of Bio-MgO NPs (50–250 μg mL^{-1}) with DPPH for 20 min at room temperature, the absorbance intensity change was detected at 517 nm (Fig. 8b and Table S2, ESI†). The results reveal that the free radical scavenging activity is directly related to the dose-dependent antioxidant effect. The Bio-MgO NPs synthesized at different plant extract concentrations 10, 20, 30, and 40 mL showed potent free radical scavenging activities of 60.8–84.2%, 71.9–89.9%, 75.8–91%, and 79.8–93.9%, respectively. Ascorbic acid as a positive control showed scavenging activity of free radicals (82–96%). The negative controls Chem-MgO and the plant extract showed free radical scavenging activities 57.5–81.8% and 59.2–83.3%, respectively (Table S2, ESI†). The half-maximal inhibitory concentration (IC$_{50}$) value represents the concentration of a sample required to inhibit 50% of the DPPH free radicals. A lower IC$_{50}$ value indicates higher antioxidant potency. IC$_{50}$ values for ascorbic acid and for other samples are shown in Fig. 8c. The results suggest that Bio-MgO NPs have a relatively potent free radical scavenging activity, though not as strong as ascorbic acid.

The peroxide scavenging activity of Bio-MgO NPs was also tested using hydrogen peroxide (H$_2$O$_2$) assay using ascorbic acid as a positive control and Chem-MgO NPs and the plant extract as negative controls (Fig. 8d and Table S3, ESI†). The Bio-MgO NPs (10, 20, 30, and 40 mL) demonstrated strong scavenging activities ranging from 64.8–82.5%, 67.7–85.3%, 71.5–86.3%, and 75.5–89.3%, respectively against H$_2$O$_2$. Ascorbic acid showed 78.5–90.3% scavenging activities and Chem-MgO and the plant extract showed 62.2–75.6% and 63.3–77.2% scavenging activities, respectively (Table S3, ESI†). The scavenging activity increases with the concentration for all samples, with Bio-MgO NPs and ascorbic acid showing the highest ROS scavenging efficiency. IC$_{50}$ values of the samples were calculated and are shown in Fig. 8e. As with the DPPH assay, ascorbic acid likely exhibits the lowest IC$_{50}$, indicating the highest potency, followed by Bio-MgO NPs. Other samples, including Chem-MgO and the plant extract, have higher IC$_{50}$ values, suggesting lower effectiveness. In general, both free radical and peroxide scavenging activities of Bio-MgO NPs showed dose-dependent antioxidant activity. In comparison with the control (ascorbic acid), Bio-MgO NPs showed promising antioxidant activity. As compared to the Chem-MgO NPs and the aqueous plant extract, Bio-MgO NPs showed enhanced free radical and ROS scavenging activities, which could be due to the synergistic activities of MgO NPs and the plant extract. Overall, results revealed that Bio-MgO NPs could serve as potent nanoplatforms to effectively scavenge free radicals and ROS.

4. Conclusions

This study successfully demonstrates the biogenic synthesis of Bio-MgO NPs using the *Verbascum sinaiticum* leaf extract as a renewable, eco-friendly reducing and stabilizing agent. The synthesis is straightforward, cost-effective, and scalable, making it

suitable for practical applications across diverse applications. The synthesized Bio-MgO NPs were thoroughly characterized using advanced techniques such as XRD, SEM, UV-visible spectroscopy, FTIR spectroscopy, TGA, DSC, and BET analysis, confirming their structural and functional properties. Remarkably, Bio-MgO NPs exhibited superior antibacterial activity at relatively low concentrations compared to Chem-MgO NPs and the crude plant extract alone. This highlights their potential as effective agents in combating bacterial infections, including those causing selected human pathogenic diseases. Furthermore, the antioxidant potential of Bio-MgO NPs was explored through DPPH and hydrogen peroxide scavenging assays, demonstrating activity comparable to that of the standard antioxidant, ascorbic acid. These findings underscore the dual benefits of Bio-MgO NPs, offering both antibacterial and antioxidant capabilities. In general, Bio-MgO NPs showed a promising solution for applications in antibacterial therapies and oxidative stress management. Their biocompatibility, cost-effectiveness, and strong bioactivity make them valuable candidates for future research and practical implementations in healthcare and environmental fields.

Author contributions

Data availability

The data supporting this article have been included as part of the ESI.†

Conflicts of interest

The authors declare no conflict of interest.

Acknowledgements

References

1 G. S. El-Sayyad, F. M. Mosallam and A. I. El-Batal, *Adv. Powder Technol.*, 2018, **29**, 2616–2625.
2 A. Lateef, S. A. Ojo, J. A. Elegbede, M. A. Azeez, T. A. Yekeen and A. Akinboro, *J. Cluster Sci.*, 2017, **28**, 1379–1392.

3 C. Kaittanis, S. Santra and J. M. Perez, *Adv. Drug Delivery Rev.*, 2010, **62**, 408–423.

4 K. M. O'Connell, J. T. Hodgkinson, H. F. Sore, M. Welch, G. P. Salmond and D. R. Spring, *Angew. Chem., Int. Ed.*, 2013, **52**, 10706–10733.

5 H. C. Neu, *Science*, 1992, **257**, 1064–1073.

6 I. Gulcin, M. Elmastas and H. Y. Aboul-Enein, *Phytother. Res.*, 2007, **21**, 354–361.

7 K. Dehvari, S. H. Chiu, J. S. Lin, W. M. Girma, Y. C. Ling and J. Y. Chang, *Acta Biomater.*, 2020, **114**, 343–357.

8 Y. Chen, R. Luo, J. Li, S. Wang, J. Ding, K. Zhao, B. Lu and W. Zhou, *ACS Nano*, 2022, **16**, 2429–2441.

9 H.-F. Chang and L.-L. Yang, *J. Med. Plants Res.*, 2012, **6**, 997–1006.

10 C. Xin, J. H. Ma, C. J. Tan, Z. Yang, F. Ye, C. Long, S. Ye and D. B. Hou, *J. Biosci. Bioeng.*, 2015, **119**, 446–454.

11 S. M. Dizaj, F. Lotfipour, M. Barzegar-Jalali, M. H. Zarrintan and K. Adibkia, *Mater. Sci. Eng., C*, 2014, **44**, 278–284.

12 Y. H. Leung, A. M. Ng, X. Xu, Z. Shen, L. A. Gethings, M. T. Wong, C. M. Chan, M. Y. Guo, Y. H. Ng, A. B. Djurisic, P. K. Lee, W. K. Chan, L. H. Yu, D. L. Phillips, A. P. Ma and F. C. Leung, *Small*, 2014, **10**, 1171–1183.

13 E. Vidhya, S. Vijayakumar, M. Nilavukkarasi, V. Punitha, S. Snega and P. Praseetha, *Mater. Today: Proc.*, 2021, **45**, 5579–5583.

14 M. Fernandes, K. R. B. Singh, T. Sarkar, P. Singh and R. Pratap Singh, *Adv. Mater. Lett.*, 2020, **11**, 1–10.

15 Y. Xie, Y. He, P. L. Irwin, T. Jin and X. Shi, *Appl. Environ. Microbiol.*, 2011, **77**, 2325–2331.

16 G. Sharma, R. Soni and N. D. Jasuja, *J. Taibah Univ. Med. Sci.*, 2017, **11**, 471–477.

17 A. E. Ferenji, Y. E. Hassen, S. L. Mekuria and W. M. Girma, *Heliyon*, 2024, **10**, e31669.

18 Y. E. Hassen, G. Gedda, A. H. Assen, D. M. Kabtamu and W. M. Girma, *ACS Omega*, 2023, **8**, 17209–17219.

19 D. Ashmore, A. Chaudhari, B. Barlow, B. Barlow, T. Harper, K. Vig, M. Miller, S. Singh, E. Nelson and S. Pillai, *Rev. Inst. Med. Trop. Sao Paulo*, 2018, **60**, e18.

20 A. Karakoti, S. Singh, J. M. Dowding, S. Seal and W. T. Self, *Chem. Soc. Rev.*, 2010, **39**, 4422–4432.

21 Y. Liu, Z. Xiao, F. Chen, L. Yue, H. Zou, J. Lyu and Z. Wang, *Sci. Total Environ*, 2021, **780**, 146578.

22 D. Wang, L. Zhao, H. Ma, H. Zhang and L.-H. Guo, *Environ. Sci. Technol.*, 2017, **51**, 10137–10145.

23 R. A. Kingsley and A. J. Baumler, *Mol. Microbiol.*, 2000, **36**, 1006–1014.

24 R. Dobrucka, *Iran. J. Sci. Technol., Trans. A: Sci.*, 2018, **42**, 547–555.

25 G. Hikku, K. Jeyasubramanian and S. V. Kumar, *J. Ind. Eng. Chem.*, 2017, **52**, 168–178.

26 Z.-X. Tang and B.-F. Lv, *Braz. J. Chem. Eng.*, 2014, **31**, 591–601.

27 M. A. Parizi, Y. Moradpour, A. Roostaei, M. Khani, M. Negahdari and G. Rahimi, *Eur. J. Exp. Biol.*, 2014, **4**, 151–156.

28 M. Elgindi, T. Mabry, F. Melek and T. Miyase, *Asian J. Chem.*, 1999, **11**, 1534–1536.

29 M. A. Ammulu, K. Vinay Viswanath, A. K. Giduturi, P. K. Vemuri, U. Mangamuri and S. Poda, *J. Genet. Eng. Biotechnol.*, 2021, **19**, 21.

30 V. V. Makarov, A. J. Love, O. V. Sinitsyna, S. S. Makarova, I. V. Yaminsky, M. E. Taliansky and N. O. Kalinina, *Acta Nat.*, 2014, **6**, 35–44.

31 H. Ryu, *Nanoscale Res. Lett.*, 2016, **11**, 36.

32 P. S. M. Kumar, A. P. Francis and T. Devasena, *J. Environ. Nanotechnol.*, 2014, **3**, 73–81.

33 Y. Dinakarkumar, C. Masi, J. R. Rajabathar, G. Ramakrishnan, R. Ninawe, H. Al-Lohedan and H. M. Veera, *J. Mol. Struct.*, 2024, **1310**, 138307.

34 S. M. Mahmoud, N. S. Abdel-Azim, A. A. Shahat, S. I. Ismail and F. M. Hammouda, *Nat. Prod. Sci.*, 2007, **13**, 186–189.

35 S. Umer, K. Asres and C. Veeresham, *Pharm. Biol.*, 2010, **48**, 461–468.

36 J. M. Geyesa, T. B. Esho, B. A. Legesse and A. S. Wotango, *Heliyon*, 2024, **10**, e24215.

37 M. Asefa, N. Teshome and A. Degu, *J. Inflammation Res.*, 2022, **15**, 6381–6392.

38 K. Lulseged, M. Z. Akele, A. A. Abiye, B. Abebe and S. Assefa Huluka, *J. Evidence-Based Complementary Altern. Med.*, 2022, 9836773.

39 B. Dereje, A. Nardos, J. Abdela, L. Terefe, M. Arega, T. M. Yilma and T. Tesfaye, *J. Exp. Pharmacol.*, 2023, **15**, 423–436.

40 T. Shanmugasundaram and R. Balagurunathan, *Artif. Cells, Nanomed., Biotechnol.*, 2017, **45**, 1521–1529.

41 J. Suresh, R. Yuvakkumar, M. Sundrarajan and S. I. Hong, *Adv. Mater. Res.*, 2014, **952**, 141–144.

42 A. M. E. Shafey, *Green Process. Synth.*, 2020, **9**, 304–339.

43 J. Singh, T. Dutta, K.-H. Kim, M. Rawat, P. Samddar and P. Kumar, *J. Nanobiotechnol.*, 2018, **16**, 1–24.

44 M. Yimer, S. N. Ansari, B. A. Berehe, K. K. Gudimella, G. Gedda, W. M. Girma, N. Hasan and S. Tasneem, *BMC Chem.*, 2024, **18**, 23.

45 A. E. Ferenj, D. M. Kabtamu, A. H. Assen, G. Gedda, A. A. Muhabie, M. Berrada and W. M. Girma, *ACS Omega*, 2024, **9**, 6803–6814.

46 P. Tiwari, B. Kumar, M. Kaur, G. Kaur and H. Kaur, *Int. Pharm. Sci.*, 2011, **1**, 98–106.

47 S. Brunauer, P. H. Emmett and E. Teller, *J. Am. Chem. Soc.*, 1938, **60**, 309–319.

48 E. P. Barrett, L. G. Joyner and P. P. Halenda, *J. Am. Chem. Soc.*, 1951, **73**, 373–380.

49 A. K. Mittal, Y. Chisti and U. C. Banerjee, *Biotechnol. Adv.*, 2013, **31**, 346–356.

50 D. Zhao, J. Feng, Q. Huo, N. Melosh, G. H. Fredrickson, B. F. Chmelka and G. D. Stucky, *Science*, 1998, **279**, 548–552.

51 G. Gedda, S. A. Sankaranarayanan, C. L. Putta, K. K. Gudimella, A. K. Rengan and W. M. Girma, *Sci. Rep.*, 2023, **13**, 6371.

52 Y. H. Leung, A. M. Ng, X. Xu, Z. Shen, L. A. Gethings, M. T. Wong, C. M. Chan, M. Y. Guo, Y. H. Ng and A. B. Djurišić, *Small*, 2014, **10**, 1171–1183.

53 Y. He, S. Ingudam, S. Reed, A. Gehring, T. P. Strobaugh, Jr. and P. Irwin, *J. Nanobiotechnol.*, 2016, **14**, 54.

54 J.-C. Kung, Y.-J. Chen, Y.-C. Chiang, C.-L. Lee, Y.-T. Yang-Wang, C.-C. Hung and C.-J. Shih, *J. Non-Cryst. Solids*, 2018, **502**, 62–70.

55 G. Sharmila, R. S. Pradeep, K. Sandiya, S. Santhiya, C. Muthukumaran, J. Jeyanthi, N. M. Kumar and M. Thirumarimurugan, *J. Mol. Struct.*, 2018, **1165**, 288–292.

56 M. I. Nabila and K. Kannabiran, *Biocatal. Agric. Biotechnol.*, 2018, **15**, 56–62.

57 A. Muhaymin, H. E. A. Mohamed, K. Hkiri, A. Safdar, S. Azizi and M. Maaza, *Sci. Rep.*, 2024, **14**, 20135.

58 R. Katwal, H. Kaur, G. Sharma, M. Naushad and D. Pathania, *J. Ind. Eng. Chem.*, 2015, **31**, 173–184.